On adhesive and buckling instabilities in the mechanics of carbon nanotubes bundles

Xuance Zhou[a], Oliver M. O'Reilly[a,]

[a]*Department of Mechanical Engineering, University of California at Berkeley, Berkeley CA 94720-1740, USA. Tel.: +510-642-0877, Fax: +510-643-5599.*

Abstract

Many recently synthesized materials feature aligned arrays or bundles of carbon nanotubes (CNTs) whose mechanical properties are partially determined by the van der Waals interactions between adjacent tubes. Of particular interest in this paper are instances where the resulting interaction between a pair of CNTs often produces a fork-like structure. The mechanical properties of this structure are noticeably different from those for isolated individual CNTs. In particular, while one anticipates buckling phenomena in the forked structure, an adhesion instability may also be present. New criteria for buckling and adhesion instabilities in fork-like structures are presented in this paper. The criteria are illuminated with a bifurcation analyses of the response of the fork-like structure to applied compressive and shear loadings.

Keywords: Carbon nanotubes, Adhesion, van der Waals interactions, Rod theory, Stability, Bifurcation, Variation, Optimization, Buckling

1. Introduction

Carbon nanotubes (CNTs), due to their high Young's modulus, low density [1], and unique opto-electrical properties [2], show great promise for applications such as thermal switches [3], nano-scale sensors [4], hard disks [5], and flat panel displays [6]. Concomitant research on the mechanical properties of a single CNT include a range of modeling and simulation works ranging from atomic [7, 8], to continuum [9, 10] and multi-scale [11]. One of the challenges in modeling CNTs is to incorporate the effects of van der Waals interactions between the CNTs. This interaction contributes to the complex, intertwined structure of curved CNTs. Understanding these interactions and how they effect the macroscopic mechanical properties and the buckling strength of the resulting arrays is of great interest (see, e.g., [12, 13, 14, 15]).

While the majority of research focuses on the strength and buckling of a single CNT [16, 17, 18] and bundles of nanotubes [13], in this paper we examine the interplay between van der Waals interactions among CNTs and classical buckling instabilities. Among our main results, we show how adhesion can produce a fork-like structure featuring a pair of CNTs and how this structure has both an improved resistance to buckling under compressive loading and an increased stiffness to shear loading compared to a single CNT. We also demonstrate an instability of the fork-like structure to perturbations in the adhered length (see Figure 2). Such an instability leads to fracture and a pair of isolated CNTs.

The paper is organized as follows: In the next section, Section 2, a model for the CNT pair shown in Figure 2 is established using rod theory, and the corresponding governing equations

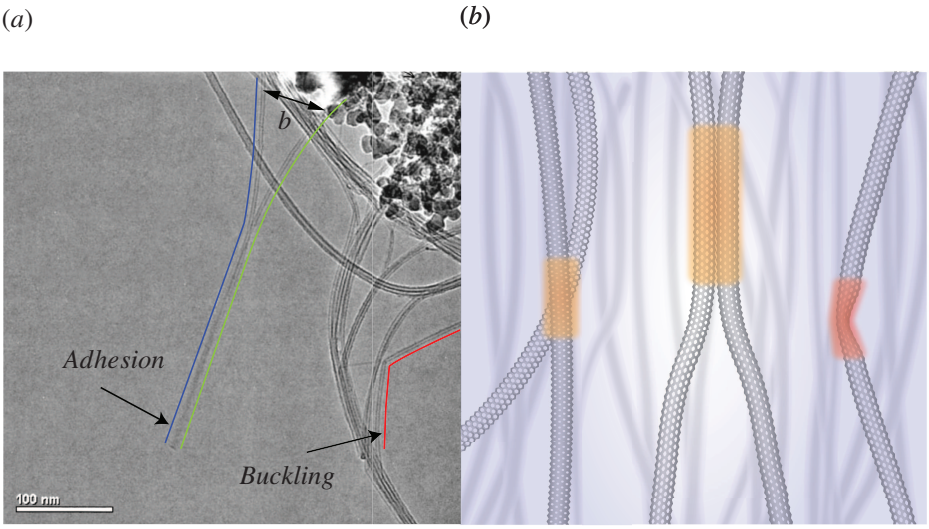

Figure 1: *(a) TEM image of carbon nanotubes grown by chemical vapor deposition. (b) Illustration of carbon nanotubes adhered by van der Waals interactions and kinked carbon nanotubes.*

for the forked configuration shown in Figure 3 are derived using variational principles. With the help of developments in [19, 20, 21, 22], we then establish nonlinear stability criteria for the forked CNT structure. In Section 3, numerical integrations of the equations governing the static configuration of the forked structure are analyzed. Our analysis demonstrates the interplay between base separation, adhesion, and terminal loading on the deformed shape of the fork-like CNT structure. Furthermore, a comprehensive investigation on the stability and bifurcations of this structure in Sections 4 and 5 leads us to appreciate the van der Waals interactions on a deeper depth. With a view towards establish design guidelines for arrays of CNTs, we conclude the paper with a discussion of the forked structure's mechanical properties in Section 6.

2. A Simple Model of an Adhered CNT Pair

To establish a feasible model for the structure shown in Figure 3 and the length scales of interest, we model each nanotube as an inextensible, flexible elastic rod which is anchored to a substrate at one end while the other end is free to adhere to the adjacent tube. The rod theory we use is classical and employed by Euler in his examination of the elastica [23, Ch. XIX]. The discussion in Love's classic text [23] is supplemented by material on branching, adhesion and material momentum from recent works (see [19, 22, 24, 25] and references therein). Referring to Figure 4, the centerline of the rod is parameterized by an arc-length coordinate $s \in [0, \ell]$ and the position of a point on the centerline is denoted by the vector-valued function $\mathbf{r}(s)$. The rod is assumed to be uniform of length ℓ with a flexural rigidity EI, mass per unit length ρ, and an adhesion energy per unit length W_{ad} when two rods are in contact with each other.

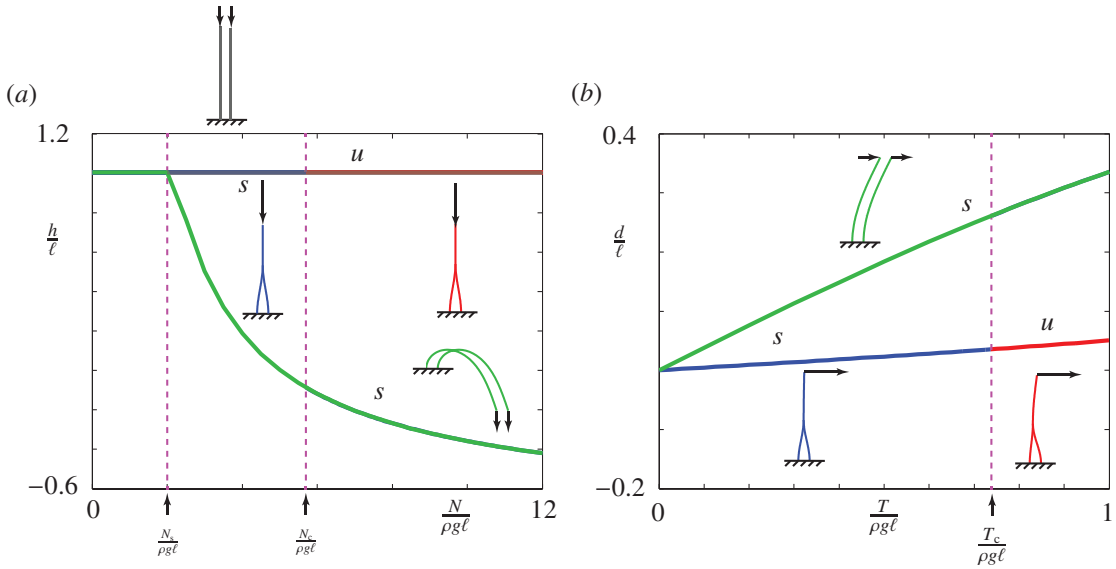

Figure 2: *Bifurcation diagram showing the deviation of the tips of the CNT pair loaded under self-weight and a terminal load* $\mathbf{F}_\ell$. *The corresponding results for a pair of unadhered CNTs are also shown. (a) The height* h *of the tips when* $\mathbf{F}_\ell = -2N\mathbf{E}_2$ *and* N *varies from* 0 *to* $12\rho g\ell$. *(b) The tangential displacement* d *of the tips when* $\mathbf{F}_\ell = 2T\mathbf{E}_1$ *and* T *varies from* 0 *to* $\rho g\ell$. *For the results shown,* $D = 1$, $\omega = 1$, *and* $\frac{b}{\ell} = 0.1$. *The labels* s *and* u *indicate stability and instability, respectively. The forces* N_c *and* T_s *are the critical normal and tangential critical loads for the forked structure, respectively, while* N_s *is the critical normal buckling load for a single CNT.*

2.1. Background

The position vector of the material point at $s = s_1$ on the centerline of the rod has the representation

$$\mathbf{r}(s = s_1) = X(s = s_1)\,\mathbf{E}_1 + Y(s = s_1)\,\mathbf{E}_2, \tag{1}$$

where the Cartesian coordinates X and Y can be defined in the standard manner:

$$\begin{aligned} X(s = s_1) &= X(s = 0) + \int_0^{s_1} \cos(\theta(\xi))\mathrm{d}\xi\,, \\ Y(s = s_1) &= Y(s = 0) + \int_0^{s_1} \sin(\theta(\xi))\mathrm{d}\xi\,. \end{aligned} \tag{2}$$

In (2), the angle θ is defined as the angle that the unit tangent vector $\mathbf{r}'$ makes with the horizontal ($\mathbf{E}_1$) direction:

$$\mathbf{r}' = \cos(\theta(s))\mathbf{E}_1 + \sin(\theta(s))\mathbf{E}_2. \tag{3}$$

Here, the prime denotes the partial derivative with respect to s. We adopt the standard assumption that $\mathbf{r}$ is continuous (i.e., there are no breaks in the rod). As a result, θ and $\mathbf{r}'$ will also be continuous functions of s (i.e., there are no kinks in the rod).

The jump in an arbitrary function $\chi = \chi(s, \theta(s), \theta'(s))$ at the point $s = \zeta$ is represented using a compact notation:

$$[\![\chi]\!]_\zeta = \chi^+ - \chi^-, \tag{4}$$

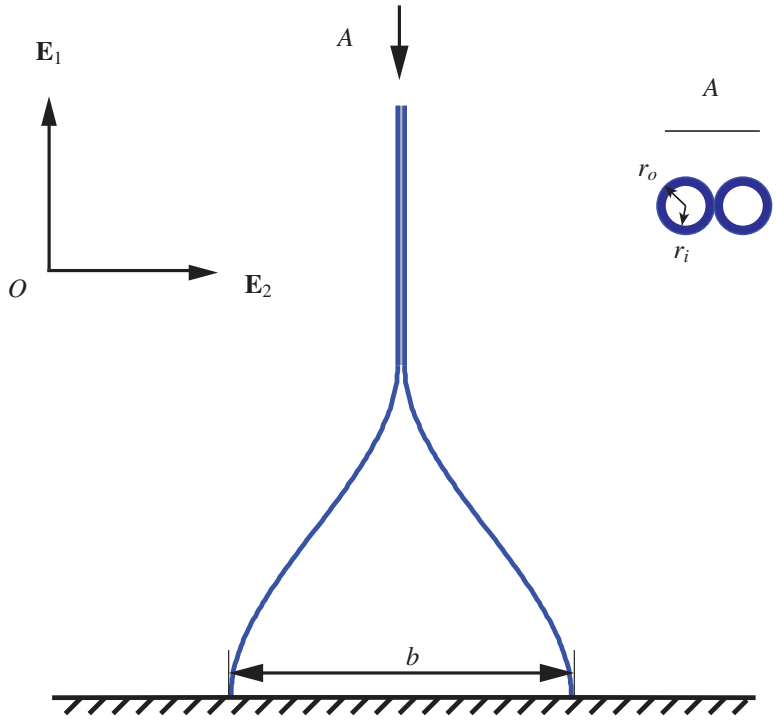

Figure 3: *Illustration of a forked structure consisting of a CNT pair. The model is based on Figure 1 and features a separation width of b at the base and an upper portion where the individual CNTs adhere to each other with the help of weak van der Waals interactions. We encourage the reader to note the top view of the CNT pair which is denoted by "A".*

where

$$\chi^- = \chi(\zeta^-) = \lim_{s \nearrow \zeta} \chi\left(s, \theta(s), \theta'(s)\right), \qquad \chi^+ = \chi(\zeta^+) = \lim_{s \searrow \zeta} \chi\left(s, \theta(s), \theta'(s)\right). \tag{5}$$

Throughout the paper, jumps in fields will be associated with points of application of forces, moments, and energies at discrete points along the rod.

The bending moment $\mathbf{m}$ and contact material force C in the rod are prescribed by well-known constitutive relations:

$$\mathbf{m} = EI\theta'\mathbf{E}_3, \qquad \mathsf{C} = \frac{EI}{2}\left(\theta'\right)^2 - \mathbf{n}\cdot\mathbf{r}' - \mathbf{m}\cdot\theta'\mathbf{E}_3, \tag{6}$$

where, assuming inner r_i and outer r_0 radii of the tube,

$$EI = E\frac{\pi}{2}\left(r_o^4 - r_i^4\right) \tag{7}$$

is the flexural rigidity and $\mathbf{n}$ is the contact force in the rod. In addition to a gravitational force $-\rho g\mathbf{E}_2$ per unit length and terminal loads acting at the ends of the rod, we also need to allow for the possibility of a singular force $\mathbf{F}_\gamma$, a singular moment $\mathbf{M}_\gamma$ and a singular supply of material momentum B_γ acting at $s = \gamma$ (cf. Figure 4). The latter supply will be related to the adhesion energy W_{ad}. The governing equations for the rod are obtained from balances of material, linear

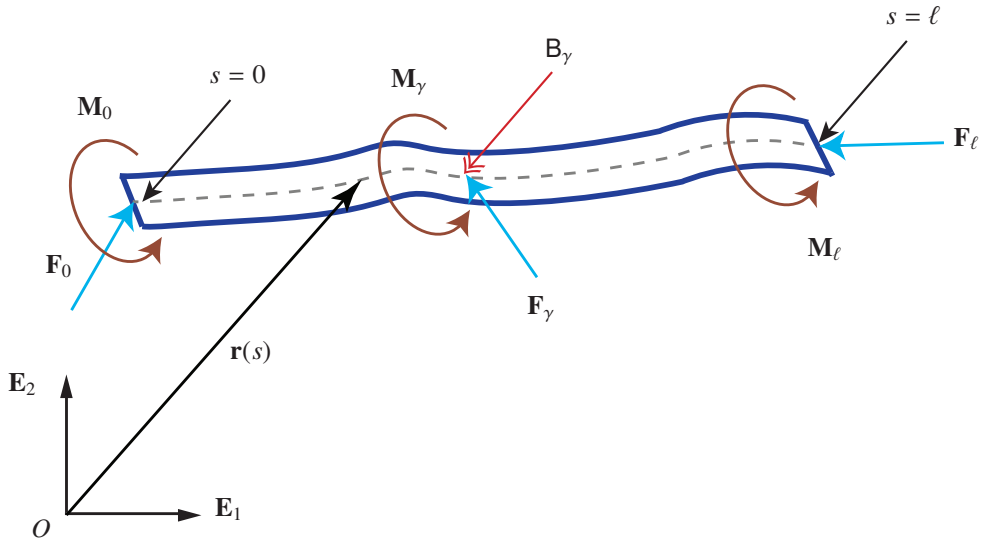

Figure 4: *Schematic representation of an elastica of length ℓ showing the position $\mathbf{r}$ of a point on the centerline. The rod is subject to a terminal force $\mathbf{F}_0$ and terminal moment $\mathbf{M}_0$ at $s = 0$, a terminal force $\mathbf{F}_\ell$ and terminal moment $\mathbf{M}_\ell$ at the end $s = \ell$, and a force $\mathbf{F}_\gamma$, material momentum supply B_γ, and moment $\mathbf{M}_\gamma$ at the point $s = \gamma$.*

and angular momenta in a standard manner:[1]

$$\begin{aligned}
\mathbf{n}' - \rho g \mathbf{E}_2 &= \mathbf{0}, \\
\frac{d}{ds}\left(EI\theta'\right) + n_2\cos(\theta) - n_1\sin(\theta) &= 0, \\
[\![\mathsf{C}]\!]_\gamma + \mathsf{B}_\gamma &= 0, \\
[\![\mathbf{n}]\!]_\gamma + \mathbf{F}_\gamma &= \mathbf{0}, \\
[\![\mathbf{m}]\!]_\gamma + \mathbf{M}_\gamma &= \mathbf{0}.
\end{aligned} \tag{8}$$

In the second of these balances, the contact force $\mathbf{n}$ has the representation $\mathbf{n} = n_1\mathbf{E}_1 + n_2\mathbf{E}_2$.

We are now in a position to develop a model consisting of three distinct rod sections connected by boundary conditions. For the first rod section, which is shown in Figure 5(b), the arc-length parameter $s_1 \in [0, \gamma)$ while for the second rod section, which is shown in Figure 5(d), $s_2 \in [0, \gamma)$. The third section, which is shown in Figure 5(c), corresponds to the adhered section of the CNT pair treated as one single rod section and the arc-length parameter for this section $s \in (\gamma, \ell]$. We assume that the two CNTs have identical moments of area I and elastic moduli E. It can be shown that the corresponding flexural rigidity for the adhered section $s \in [\gamma, \ell]$ is $10EI$.

The fields and variables associated with the first section of the fork structure are labelled with a subscript 1, those for the second section are labelled with a subscript 2, and those for the adhered section aren't distinguished with a subscript. To describe conditions at the branching point γ, we generalize our earlier notation for a jump condition in an obvious manner:

$$[\![\chi]\!]_\gamma = \chi^+ - \chi_1^- - \chi_2^-. \tag{9}$$

[1]The reader is referred to [19] and [25] for further details on the role played by material momentum. We note in particular that $(8)_3$ leads to an adhesion boundary condition.

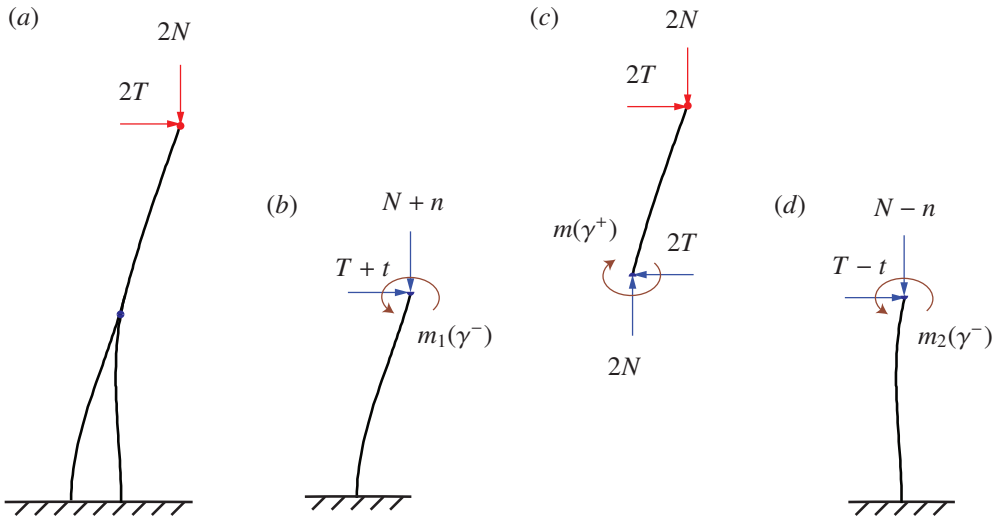

Figure 5: *Some of the forces on the components of the model for the CNT pair. (a) Terminal loading at $s = \ell$ for the CNT pair system. (b) Terminal loading at $s = \gamma^-$ for the first CNT. (c) Terminal loading at $s = \gamma^+$ and $s = \ell$ for the adhered portion of the model. (d) Terminal loading at $s = \gamma^-$ for the second CNT. Here, $m = EI\theta'$, and t and n represent the difference of the internal forces at $s = \gamma$ between the two CNTs (cf. (12)).*

At the junction $s = \gamma$ for the three rod segments, we have the following continuity (branching) conditions:

$$[\![\mathbf{n}]\!]_\gamma = \mathbf{0}, \qquad [\![\mathbf{m}]\!]_\gamma = \mathbf{0}, \qquad [\![\mathsf{C}]\!]_\gamma + \mathsf{B}_\gamma = 0. \tag{10}$$

The second and third of these conditions will appear later from a variational principle and the supply B_γ is related to the adhesion energy: $\mathsf{B}_\gamma = -W_{\text{ad}}$.

2.2. *Governing Equations*

From the governing equations for the adhered portion of the structure, we find that

$$\begin{aligned} \mathbf{n}(\ell^-) &= 2T\mathbf{E}_1 - 2N\mathbf{E}_2, \\ \mathbf{n}(\gamma^+) &= 2T\mathbf{E}_1 - (2N + 2\rho g(\ell - \gamma))\,\mathbf{E}_2. \end{aligned} \tag{11}$$

The branching condition $(10)_1$ at $\xi = \gamma$ shows how the contact force $\mathbf{n}(\gamma^+)$ distributes upstream into the two segments. By defining the pair of variables t, n characterizing the difference in the contact force between the two rods at $s_1 = \gamma$ and $s_2 = \gamma$, the contact forces in each rod can be expressed in an illuminating manner:

$$\begin{aligned} \mathbf{n}_1(\gamma^-) &= (T + t)\mathbf{E}_1 - (N + \rho g(\ell - \gamma) + n)\,\mathbf{E}_2, \\ \mathbf{n}_2(\gamma^-) &= (T - t)\mathbf{E}_1 - (N + \rho g(\ell - \gamma) - n)\,\mathbf{E}_2. \end{aligned} \tag{12}$$

The balance law $(8)_1$ applied to the appropriate segment can be used to determine $\mathbf{n}_1(s_1)$ and $\mathbf{n}_2(s_2)$, respectively.

Recalling that the total energy of the rods consists of the sum of the strain energy, gravitational potential energy and the potential energy of the terminal load, it is straightforward to show

that the potential energy of the structure is

$$\pi = \int_{\gamma}^{\ell} f \mathrm{d}s + \sum_{J=1}^{2} \int_{0}^{\gamma} f_J \mathrm{d}s_J, \tag{13}$$

where

$$\begin{aligned} f &= 5EI\left(\theta'\right)^2 + (2\rho g(\ell - s) + 2N)\sin(\theta) - 2T\cos(\theta) - W_{\mathrm{ad}}, \\ f_1 &= \frac{EI}{2}\left(\theta_1'\right)^2 + (\rho g(\ell - s) + N + n)\sin(\theta_1) - (T + t)\cos(\theta_1), \\ f_2 &= \frac{EI}{2}\left(\theta_2'\right)^2 + (\rho g(\ell - s) + N - n)\sin(\theta_2) - (T - t)\cos(\theta_2). \end{aligned} \tag{14}$$

Variations of π feature variations in γ, $\theta_1(s_1)$, $\theta_2(s_2)$, and $\theta(s)$. These variations are denoted by $\epsilon\mu$, $\epsilon\eta_1(s_1)$, $\epsilon\eta_2(s_2)$, and $\epsilon\eta(s)$, respectively. It is straightforward to show that the variations satisfy a set of compatibility conditions based on continuity at $s = \gamma$:[2]

$$\begin{aligned} \left(\mu\theta' + \eta\right)^{+} &= \left(\mu\theta_1' + \eta_1\right)^{-} = \left(\mu\theta_2' + \eta_2\right)^{-}, \\ \left(\mu^2\theta'' + 2\mu\eta\right)^{+} &= \left(\mu^2\theta_1'' + 2\mu\eta_1\right)^{-} = \left(\mu^2\theta_2'' + 2\mu\eta_2\right)^{-}. \end{aligned} \tag{15}$$

We also note the boundary conditions on the variations,

$$\eta'(\ell) = 0, \qquad \eta_1(s_1 = 0) = 0, \qquad \eta_2(s_2 = 0) = 0, \tag{16}$$

which follow from the moment free-loading at $s = \ell$ and the clamped boundary conditions at the base of the CNTs, respectively.

Either by using (8) and (10) or by computing the first variation of π and invoking $(16)_{2,3}$,

$$\begin{aligned} \left.\frac{\mathrm{d}\pi}{\mathrm{d}\epsilon}\right|_{\epsilon=0} = -\mu\left[\!\left[f\right]\!\right]_{\gamma} &+ \int_{\gamma}^{\ell}\left\{\frac{\partial f}{\partial\theta} - \frac{\mathrm{d}}{\mathrm{d}s}\left(\frac{\partial f}{\partial\theta'}\right)\right\}\eta\mathrm{d}s + \eta\left.\frac{\partial f}{\partial\theta'}\right|_{\ell} - \eta\left.\frac{\partial f}{\partial\theta'}\right|_{\gamma} \\ &+ \sum_{K=1}^{2}\int_{0}^{\gamma}\left\{\frac{\partial f_K}{\partial\theta_K} - \frac{\mathrm{d}}{\mathrm{d}s_K}\left(\frac{\partial f_K}{\partial\theta_K'}\right)\right\}\eta_K\mathrm{d}s + \sum_{K=1}^{2}\eta_K\left.\frac{\partial f_K}{\partial\theta_K'}\right|_{\gamma}, \end{aligned} \tag{17}$$

we are led to the boundary-value problem for the deformed shape θ and θ_K of the CNT pairs. The resulting problem consists of three ordinary differential equations,

$$\begin{aligned} 5EI\theta'' - (\rho g(\ell - s) + N)\cos(\theta) - T\sin(\theta) &= 0, \quad s \in (\gamma^{+}, \ell), \\ EI\theta_1'' - (\rho g(\ell - s) + (N + n))\cos(\theta_1) - (T + t)\sin(\theta_1) &= 0, \quad s_1 \in (0, \gamma^{-}), \\ EI\theta_2'' - (\rho g(\ell - s) + (N - n))\cos(\theta_2) - (T - t)\sin(\theta_2) &= 0, \quad s_2 \in (0, \gamma^{-}), \end{aligned} \tag{18}$$

and is equivalent to the statement that the first variation of π is zero. The desired solution θ, θ_1, and θ_2 to (18) needs to satisfy nine conditions. These conditions pertain to the clamped boundary conditions at $s_{1,2} = 0$, continuity of θ and bending moment at the point of adhesion, the adhesion

[2] For details on how these conditions can be established, the interested reader is referred to [19] and [22].

boundary condition, the absence of a terminal moment at $s = \ell$ and a pair of isoperimetric conditions:

$$\begin{gathered}
\theta_1(0) = \frac{\pi}{2}, \quad \theta_2(0) = \frac{\pi}{2}, \\
\theta_1(\gamma^-) = \theta(\gamma^+), \quad \theta_2(\gamma^-) = \theta(\gamma^+), \\
10EI\theta'(\gamma^+) - EI\theta_1'(\gamma^-) - EI\theta_2'(\gamma^-) = 0, \\
5EI\,(\theta'(\gamma^+))^2 - \frac{EI}{2}\,(\theta_1'(\gamma^-))^2 - \frac{EI}{2}\,(\theta_2'(\gamma^-))^2 = W_{\text{ad}}, \\
\theta'(\ell) = 0, \\
\int_0^\gamma \cos(\theta_1)\mathrm{d}s - \int_0^\gamma \cos(\theta_2)\mathrm{d}s - b = 0, \\
\int_0^\gamma \sin(\theta_1)\mathrm{d}s - \int_0^\gamma \sin(\theta_2)\mathrm{d}s = 0.
\end{gathered} \tag{19}$$

The forces t and n can be interpreted as constraint forces which impose the constraints $(19)_{8,9}$. In the interests of brevity, the solution to the boundary-value problem (18) and (19) will often be denoted by an asterisk: $\theta^*(s), \theta_K^*(s_K)$, and γ^*.

In the sequel, we shall find it convenient to define a dimensionless flexural rigidity D, and adhesion energy W_{ad}:

$$D = \frac{EI}{\rho g \ell^3}, \qquad \omega = \frac{W_{\text{ad}}}{\rho g \ell}. \tag{20}$$

We shall also use the weight $\rho g \ell$ of a single CNT to non-dimensionalize the terminal load and contact force.

3. Stiffnesses of the Fork-Like Structure

Our first avenue of investigation is to examine the stiffness of the forked-structure formed by the adhered pair of CNTs. To start we consider the length b by which the clamped bases of the CNTs are separated and set the terminal loading at $s = \ell$ to zero. We expect that by increasing b from zero, the adhered length $\ell - \gamma$ should decrease from ℓ to 0. Our numerical investigations of (18) and (19), confirm that this is indeed the case. The results are summarized in Figure 6. For the parameter values shown in this figure, the adhered length $\ell - \gamma \to 0$ and $b \to 0.32\ell$.

The stiffnesses of the fork-like structure to terminal loadings such as that shown in Figure 5(a) provides a measure of the structural effectiveness of the CNT structure. To this end, we assume a terminal loading $\mathbf{n}(\ell^-) = \mathbf{F}_\ell = 2T\mathbf{E}_1 - 2N\mathbf{E}_2$ and measure the vertical deflection Δh and horizontal deflection Δd of the material point located at the tip $s = \ell$ of the adhered portion of the structure. The factor of 2 in the representation for $\mathbf{F}_\ell$ enables a ready comparison to the case of a single CNT.

It is straightforward to use the displacements Δd and Δh to define a pair of stiffnesses:

$$k_1 = \frac{\Delta\mathbf{F}_\ell \cdot \mathbf{E}_1}{\Delta d}, \qquad k_2 = \frac{\Delta\mathbf{F}_\ell \cdot \mathbf{E}_2}{\Delta h}. \tag{21}$$

For our numerical results, the shear stiffnesses k_1 and compressive stiffness k_2 are represented by the slopes in Figures 7(a) and (b), respectively. These results were obtained by numerical integrations of (18) and (19). We emphasize that, for a given b, the adhered length $\ell - \gamma$ will vary

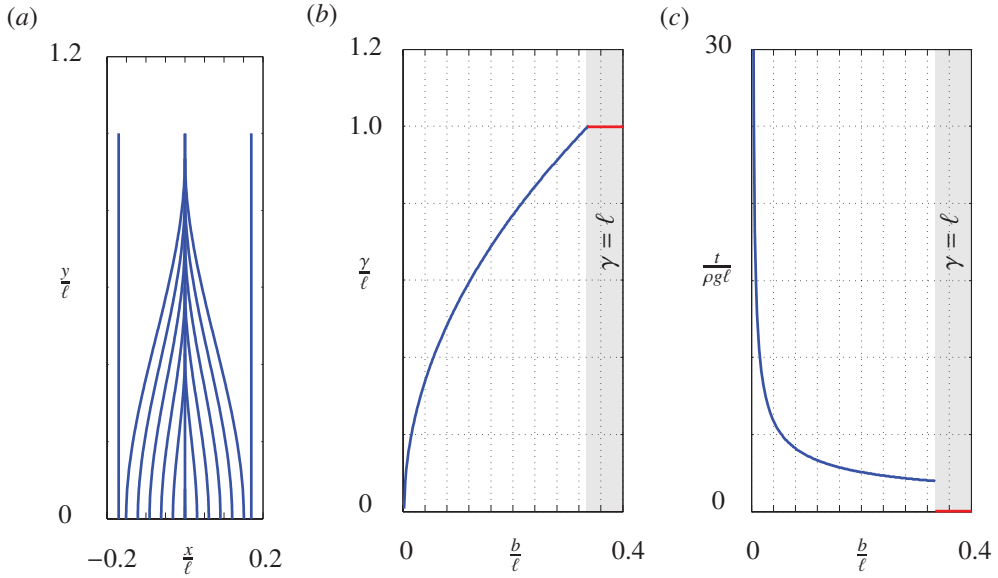

Figure 6: *Adhesion formation for a single CNT pair in the presence of its own self weight $\rho g \ell$ and in the absence of a terminal load: $\mathbf{F}_\ell = \mathbf{0}$. (a) Equilibrium configurations of the CNT pair as b varies. (b) The corresponding dimensionless detached length γ/ℓ between the two CNTs. (c) The force $t = \mathbf{n}_1(\gamma^-) \cdot \mathbf{E}_1 = -\mathbf{n}_2(\gamma^-) \cdot \mathbf{E}_1$ at the adhesion point $s = \gamma$. For the results shown, $D = 1$, $\omega = 1$, $\frac{b}{\ell} \in [0, 0.4]$, $T = 0$, and $N = 0$.*

depending on the loads T and N. Despite changes to the adhered length, for a given separation b, we observe that the stiffnesses are (surprisingly) almost constant.

Before discussing the results further, we pause to discuss the case of a single CNT. The stiffness to a shear load of $T\mathbf{E}_1$ for a single CNT is shown as the dashed line in Figure 7(a). We observe that this stiffness is lower than the corresponding stiffness for the adhered pair of CNTs. When the stiffness to a normal load $-N\mathbf{E}_2$ of a single CNT is considered, we find that the CNT is rigid for loads less than the buckling load N_s (i.e., when $N > N_s$), then the stiffness becomes very small (as shown by the dashed line in Figure 7(b)). Although the fork-like structure formed by the nanotube pair and the single CNT exhibit unequal shear and compressive stiffnesses, for the former $k_1 \gg k_2$. This is in contrast to the single CNT where the opposite inequality holds before the onset of buckling. We also note that, as the separation b increases, k_1 increases, whereas k_2 decreases. The decrease in k_2 is anticipated as this stiffness is expected to become unbounded as $b \to 0$: a straight unbuckled strut is effectively rigid to vertical loads (that are below its buckling limit). We thus note that the forked-structure makes the CNT pair more compliant to compressive loads, more resistant to buckling, and stiffer to shearing loads compared to the isolated single CNT.

4. Stability

The equilibrium configurations of the CNTs discussed in Section 3 feature large contact forces and a discontinuity at $s = \gamma$. While it is often relatively straightforward to determine these configurations, the issue of stability has not been discussed previously. We now turn to presenting stability criteria. In addition, to a buckling criterion that is similar to those in the

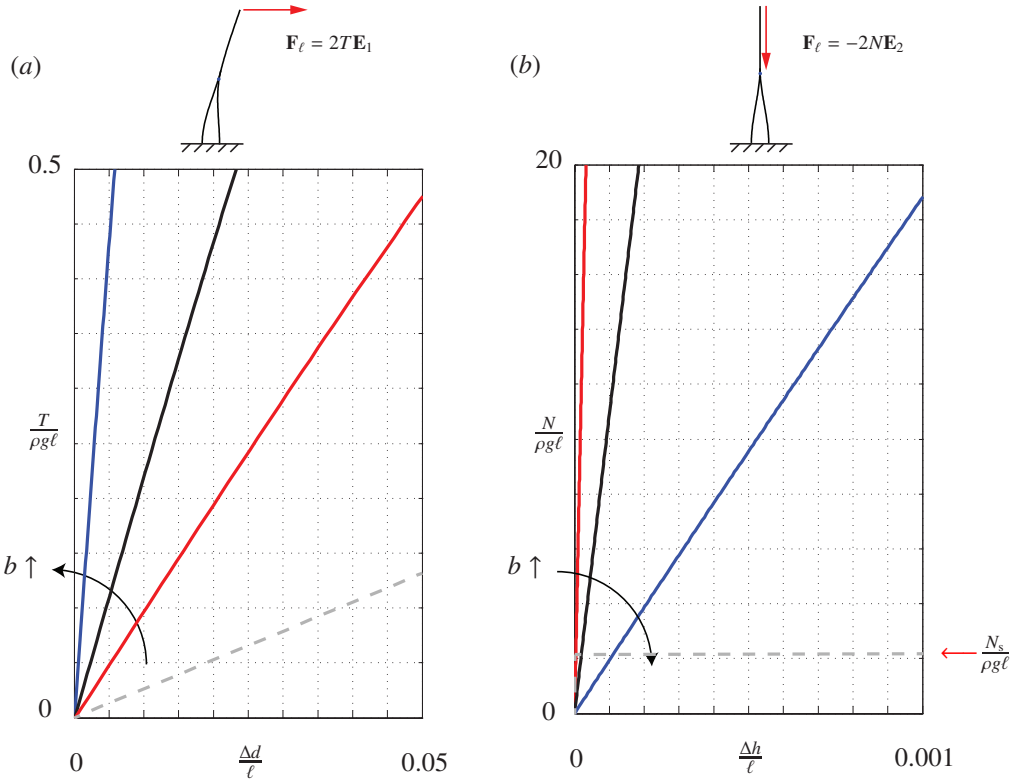

Figure 7: *The dependency of terminal load on the tip deformation for different values of the separation distance b. (a) The terminal load* $2T$ *in the horizontal direction as a function of the tip displacement* Δd *in the horizontal direction when* $\mathbf{F}_\ell = 2T\mathbf{E}_1$*. The dashed line shows the corresponding stiffness calculation for a single CNT. (b) The terminal compressive load* $2N$ *in the vertical direction as a function of the tip displacement* Δh *in the vertical direction when* $\mathbf{F}_\ell = -2N\mathbf{E}_2$*. The dashed line in this figure shows the corresponding stiffness calculation for a single CNT. For the results shown,* $D = 1$*,* $\omega = 1$*, and* $\frac{b}{\ell} = 0.05,\ 0.1,$ *and* 0.2*.*

literature for a single strut and branched tree-like structures, we also find a criterion pertaining to the stability of the adhesion. In the sequel, we find that instability manifests in adhesive failure and leads to equilibrium configurations where the CNTs are separated.

4.1. Computation of the Second Variation

To establish the criteria for stability, we compute the second variation J of the potential energy function π in Eqn. (14) by considering variations to the solution $\left\{\theta^*(s), \theta_K^*(s_K), \gamma^*\right\}$ of the boundary-value problem (18) and (19). After some rearranging, the following expression for J

is found:

$$J = \left.\frac{\mathrm{d}^2\pi}{\mathrm{d}\epsilon^2}\right|_{\epsilon=0} = \int_{\gamma^*}^{\ell}\left\{M\eta^2 + R\eta'\eta'\right\}\mathrm{d}s + \sum_{K=1}^{2}\int_0^{\gamma^*}\left\{M_K\eta_K^2 + R_K\eta_K'\eta_K'\right\}\mathrm{d}s_K$$
$$+\mu^2\left(\left(\sum_{K=1}^{2}\frac{\mathrm{d}f_K}{\mathrm{d}s_K}\right)^- - \left(\frac{\mathrm{d}f}{\mathrm{d}s}\right)^+\right) + 2\mu\left(\left(\sum_{K=1}^{2}\frac{\partial f_K}{\partial\theta_K}\eta_K\right)^- - \left(\frac{\partial f}{\partial\theta}\eta\right)^+\right)$$
$$+2\mu\left(\left(\sum_{K=1}^{2}\frac{\partial f_K}{\partial\theta_K'}\eta_K'\right)^- - \left(\frac{\partial f}{\partial\theta'}\eta'\right)^+\right). \tag{22}$$

In writing (22), we used the standard abbreviations

$$\begin{aligned} M &= -2\rho g(\ell - s)\sin(\theta^*) - 2L\sin(\theta^*), & R &= 10D,\\ M_1 &= -\rho g(\ell - s)\sin(\theta_1^*) - (L+n)\sin(\theta_1^*) + P\cos(\theta_1^*), & R_1 &= D,\\ M_2 &= -\rho g(\ell - s)\sin(\theta_2^*) - (L-n)\sin(\theta_2^*) - P\cos(\theta_2^*), & R_2 &= D. \end{aligned}$$

By careful use of the compatibility conditions (15), (22) can be decomposed into two terms:

$$J = J_0 + J_\gamma. \tag{23}$$

Here, the components of J_0 have a classical form and J_γ is entirely associated with varying the branching point $s = \gamma$:

$$\begin{aligned} J_0 &= \sum_{K=1}^{2}\int_0^{\gamma^*}\left\{M_K\eta_K^2 + R_K\eta_K'\eta_K'\right\}\mathrm{d}s_K + \int_{\gamma^*}^{\ell}\left\{M\eta^2 + R\eta'\eta'\right\}\mathrm{d}s,\\ J_\gamma &= -\mu^2 e - 2\eta(\gamma^{*+})\mu\left[\!\left[\frac{\partial f}{\partial\theta}\right]\!\right]_{\gamma^*}, \end{aligned} \tag{24}$$

where

$$e = \sum_{K=1}^{2}\left\{2\frac{\partial f_K}{\partial\theta_K}^-\left(\left(\theta^{*\prime}\right)^+ - \left(\theta_K^{*\prime}\right)^-\right) + \frac{\partial f_K}{\partial\theta_K'}^-\left(\left(\theta^{*\prime\prime}\right)^+ - \left(\theta_K^{*\prime\prime}\right)^-\right)\right\} + \left[\!\left[\frac{\mathrm{d}f}{\mathrm{d}s}\right]\!\right]_{\gamma^*}. \tag{25}$$

It is unclear if J_0 is necessarily positive and so we next follow a method attributed to Legendre and add the following term to J:

$$0 = \int_{\gamma^*}^{\ell}\frac{\mathrm{d}}{\mathrm{d}s}(\eta^2 w)ds + \sum_{K=1}^{2}\int_0^{\gamma^*}\frac{\mathrm{d}}{\mathrm{d}s}(\eta_K^2 w_K)ds_K - [\eta^2 w]_{\gamma^*}^{\ell} - \sum_{K=1}^{2}[\eta_K^2 w_K]_0^{\gamma^*}. \tag{26}$$

In order to dramatically simplify J, we require the functions $w(s)$, $w_1(s_1)$ and $w_2(s_2)$ featuring in (26) to satisfy a set of Riccati equations,

$$\begin{aligned} w' + M - \frac{w^2}{R} &= 0, & s &\in (\gamma^*, \ell),\\ w_1' + M_1 - \frac{w_1^2}{R_1} &= 0, & s_1 &\in [0, \gamma^*),\\ w_2' + M_2 - \frac{w_2^2}{R_2} &= 0, & s_2 &\in [0, \gamma^*), \end{aligned} \tag{27}$$

subject to the boundary conditions that ensure that $J \geq 0$.

The addition of (26) allows J to be decomposed into the following additive sum

$$J = J_1 + J_2 + J_3 \tag{28}$$

where

$$\begin{aligned} J_1 &= \mu^2\left(-e - \sum_{K=1}^{2}\left\langle\!\left\langle \theta^{*'}, \theta_K^{*'}\right\rangle\!\right\rangle^2 w_K\left(\gamma^{*-}\right)\right) - 2\eta\left(\gamma^{*+}\right)\mu\left(\left[\!\left[\frac{\partial f}{\partial \theta}\right]\!\right]_{\gamma^*} + \sum_{K=1}^{2}\left\langle\!\left\langle \theta^{*'}, \theta_K^{*'}\right\rangle\!\right\rangle w_K\left(\gamma^{*-}\right)\right) \\ &\quad +\eta\left(\gamma^{*+}\right)\eta\left(\gamma^{*+}\right)[\![w]\!]_{\gamma^*}, \\ J_2 &= \int_{\gamma^*}^{\ell} R\left\{\eta' + \frac{w}{R}\eta\right\}^2 ds + \sum_{K=1}^{2}\int_0^{\gamma^*} R_K\left\{\eta_K' + \frac{w_K}{R_K}\eta_K\right\}^2 ds_K, \\ J_3 &= \eta_1^2(0)w_1(0) + \eta_2^2(0)w_2(0) - \eta^2(\ell)w(\ell). \end{aligned} \tag{29}$$

In writing J_1 we use the abbreviated notation

$$\left\langle\!\left\langle \theta^{*'}, \theta_K^{*'}\right\rangle\!\right\rangle = \theta^{*'}\left(\gamma^{*+}\right) - \theta_K^{*'}\left(\gamma^{*-}\right). \tag{30}$$

Referring to $(16)_{2,3}$, because of the clamped boundary conditions at $s_1 = 0$ and $s_2 = 0$, J_3 reduces to a single term. To ensure that $J_3 = 0$ for all possible perturbations, we shall choose $w(\ell) = 0$ in the sequel. We now seek additional necessary conditions for $J = J_1 + J_2$ to be positive for a given configuration of the CNT pair. When these conditions are not satisfied we can conclude that the configuration is unstable. There will be two sets of necessary conditions. The first set will be used to determine buckling instabilities of the forked structure and the second set will be used to indicate instabilities associated with the adhesion of the CNTs.

4.2. Structural Stability: Buckling

We examine buckling in the structure by considering perturbations to the equilibrium configuration which do not perturb the adhesion point to first order. The stability criterion for this case is the easiest to obtain because $\mu = 0$ and, consequently, the positiveness of J is guaranteed provided solutions to the Riccati equations (27) can be found with $w(\ell) = 0$ which render $[\![w]\!]_{\gamma^*} \geq 0$. We thus start by integrating the Riccati equation for $w(s)$ backwards in s until we reach the branch point. Then the value $w\left(\gamma^{*+}\right)$ is used to specify $w_1\left(\gamma^{*-}\right)$ and $w_2\left(\gamma^{*-}\right)$ and the corresponding Riccati equations are integrated backwards in s_1 and s_2 until s_1 and s_2 are both zero. A successful integration should yield finite values of $w(s)$ for $s \in (\gamma^*, \ell]$ and $w_K\left(s_K\right)$ for $s_K \in (0, \gamma^*)$.

In summary,

Condition B1: *If a solution* $\left\{\theta^*(s), \theta_K^*\left(s_K\right), \gamma^*\right\}$ *to the boundary-value problem (18) and (19) minimizes* π *then the respective solutions* $w(s)$, $w_1\left(s_1\right)$, *and* $w_2\left(s_2\right)$ *to (27) with* $w(\ell) = 0$ *and* $[\![w]\!]_{\gamma^*} \geq 0$, *cannot become unbounded.*

4.3. Weak van der Waals Stability: Debonding

To examine instabilities induced by changes in γ, we now consider the effects of non-zero μ. The resulting instability criterion subsumes the earlier buckling result. With $\mu \neq 0$, we now need

to consider the term J_1 in (28). For this term's contribution to be positive for any μ and η^+, we require

$$\begin{aligned} [\![w]\!]_{\gamma^*} &\geq 0, \\ -e - \sum_{K=1}^{2} \left\langle\!\left\langle \theta^{*'}, \theta_K^{*'} \right\rangle\!\right\rangle^2 w_K(\gamma^{*-}) &\geq 0, \\ \Gamma &\geq 0. \end{aligned} \tag{31}$$

In the last of these conditions, we have defined the following function Γ for conciseness:

$$\Gamma = \left(-e - \sum_{K=1}^{2} \left\langle\!\left\langle \theta^{*'}, \theta_K^{*'} \right\rangle\!\right\rangle^2 w_K(\gamma^{*-}) \right) [\![w]\!]_{\gamma^*} - \left(\left[\!\left[\frac{\partial f}{\partial \theta} \right]\!\right]_{\gamma^*} + \sum_{K=1}^{2} \left\langle\!\left\langle \theta^{*'}, \theta_K^{*'} \right\rangle\!\right\rangle w_K(\gamma^{*-}) \right)^2 . \tag{32}$$

We note that $(31)_3$ subsumes $(31)_2$.

Hence, in summary,

Condition AB1: *If a solution* $\left\{\theta^*(s), \theta_K^*(s_K), \gamma^*\right\}$ *to the boundary-value problem (18) and (19) minimizes* π *then the respective solutions* $w(s)$, $w_1(s_1)$, *and* $w_2(s_2)$ *to (27) with* $w(\ell) = 0$ *and* $[\![w]\!]_{\gamma^*} \geq 0$, *cannot become unbounded. In addition,* $\Gamma \geq 0$.

While we say a solution $\left\{\theta^*(s), \theta_K^*(s_K), \gamma^*\right\}$ that satisfies $AB1$ is stable, and otherwise it is said to be unstable, strictly speaking we have only established a necessary condition for stability. A sufficient condition for nonlinear stability for the forked-structure remains to be found.

4.4. Implementation of the Stability Criteria

The primary difficulties in implementing the stability criteria $B1$ and $AB1$ are the conditions $[\![w]\!]_{\gamma^*} \geq 0$ and the boundedness of solutions to the Riccati equations. To help with this, we exploit the known relationship between unbounded solutions of a Riccati equation to conjugate points for a Jacobi equation [26]. It should be emphasized that the process we discuss here needs to be repeated for each solution $\left\{\theta^*(s), \theta_K^*(s_K), \gamma^*\right\}$. For convenience, and where no confusion may arise, we henceforth drop the $*$ ornamenting γ, θ, and θ_K.

First, we invoke a set of Jacobi transformations that define the three functions $u(s)$ and $u_K(s_K)$,

$$w = -R\frac{u'}{u}, \qquad w_K = -R_K\frac{u_K'}{u_K}, \tag{33}$$

and transform the Riccati equations to a set of Jacobi differential equations:

$$\begin{aligned} Ru'' - Mu = 0, \qquad u(\ell) = 0, \qquad u'(\ell) = 1, \qquad s \in (\gamma, \ell), \\ R_K u_K'' - M_K u_K = 0, \qquad s_K \in [0, \gamma). \end{aligned} \tag{34}$$

We then numerically integrate $(34)_2$ using the initial conditions

$$u_K(0) = 0, \qquad u_K'(0) = 1, \tag{35}$$

With the help of (33), the resulting solutions $u_K(s_K)$ correspond to solutions $w_K(s_K)$ to the Riccati equations that become unbounded at $s_K = 0$ (see Figure 8). We denote the latter solutions as $w_{K_{\text{cri}}}$. In particular the values of these solutions at the adhesion point are of particular importance:

$$w_{K_{\text{cri}}}^- = w_{K_{\text{cri}}}(\gamma^-). \tag{36}$$

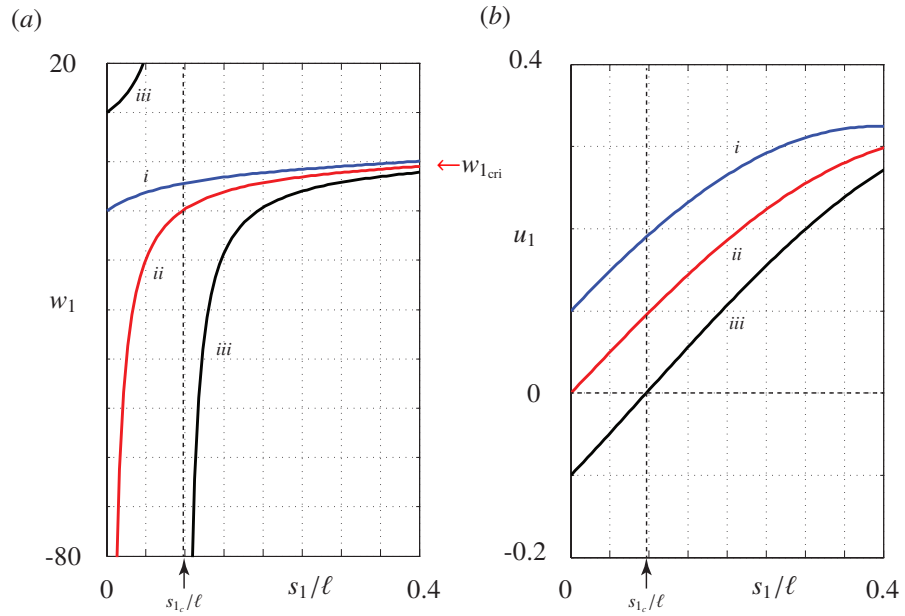

Figure 8: *Three representative solutions to (a) the Riccati differential equation (27)$_2$ and (b) the corresponding solutions to the Jacobi differential equation (34)$_{2,K=1}$. For the solutions shown, i denotes a bounded solution $w_1(s_1)$ to the Riccati equation whose counterpart $u_1(s_1)$ has no conjugate points in $s \in [0, \gamma)$, ii denotes the bounded solution $w_{1_{cri}}(s_1)$ to the Riccati equation whose counterpart $u_{1_{cri}}(s_1)$ has a conjugate points at $s_1 = 0$, and iii denotes an unbounded solution $w_1(s_1)$ to the Riccati equation whose counterpart $u_1(s_1)$ has a conjugate point at $s_{1_c} \in (0, \gamma)$.*

Our strategy is to integrate (27)$_1$ to determine $w(s)$ and then select the two initial conditions w_K^- such that the pair belongs to a set $\mathcal{F}$:

$$\mathcal{F} = \left\{ \left(w_1(\gamma^-), w_2(\gamma^-) \right) \middle| w_K(\gamma^-) > w_{K_{\text{cri}}}^-, \quad w(\gamma^+) \geq w_1(\gamma^-) + w_2(\gamma^-) \right\}. \tag{37}$$

The conditions featuring in the definition of $\mathcal{F}$ are summarized graphically in Figure 9.

If a solution $w(s)$ to (27)$_1$ can be found and then a pair of solutions to (27)$_{2,3}$ found that satisfy (37), we will have satisfied the necessary condition $B1$ for stability. To satisfy the stronger condition $AB1$, we need to be able to select the pair of initial conditions w_K^- so that $\Gamma > 0$. This selection process can be formulated as an optimization problem:

$$\max_{(w_1^-, w_2^-) \in \mathcal{F}} \Gamma. \tag{38}$$

If we find the resulting maximum value of Γ to be positive, then the condition $AB1$ is satisfied. We solve the optimization problem using the interior-point algorithm [27] implemented using the Matlab function fmincon. This algorithm sometimes provides the maximum value of Γ even in cases where the associated values of $\left(w_1^-, w_2^-\right) \notin \mathcal{F}$. We refer to such instances as unfeasible in the results presented below.

4.5. Application of the Stability Criteria B1 and AB1

We now turn to investigating the stability of the equilibrium configurations of a terminally loaded pair of CNTs which are also assumed to have a negligible self weight. To start, we first

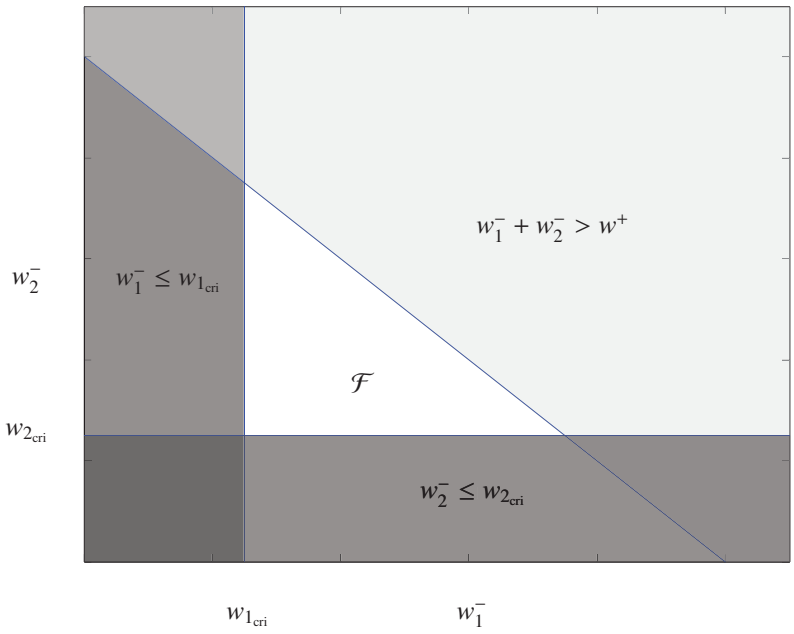

Figure 9: *Graphical illustration of the set $\mathcal{F}$ defined by (37) for the pair of initial conditions w_1^- and w_2^-.*

investigate instability as the normal load varies: $\mathbf{F}_\ell = -2N\mathbf{E}_2$. In Figure 10, we observe as the normal load N increases that the maximum Γ decreases and eventually reaches zero. Beyond this critical load, the equilibrium configuration does not satisfy $AB1$ and is hence considered unstable.

The shaded region labelled I in Figure 11 indicates areas of the $w_1^- - w_2^-$ parameter space where the maximum value of Γ found by the optimization algorithm failed to satisfy $[\![w]\!]_\gamma \geq 0$ and/or $w_K(\gamma^-) < w_{K_{\text{cri}}}^-$. That is, where $\left(w_1^-, w_2^-\right) \notin \mathcal{F}$ for the maximum value of Γ. Solutions in this parameter region are said to be unfeasible.

The situation under a shearing load $\mathbf{F}_\ell = 2T\mathbf{E}_1$ and self weight is far less stable than under the previous loading. As illustrated by the results shown in Figure 11, we find that the critical tangential load T needed to cause the instability ($\Gamma < 0$) is far less than the corresponding critical normal load N. In contrast to Figure 10, we find that the region will not immediately become infeasible when $\Gamma < 0$ which suggests that the weak van der Waals interaction becomes unstable before the onset of a buckling instability.

We next consider combined tangential and normal loading:

$$\mathbf{F}_\ell = F_\ell\left(\cos(\phi)\mathbf{E}_1 - \sin(\phi)\mathbf{E}_2\right) \tag{39}$$

where the angle ϕ ranges from $-\frac{\pi}{2}$ to $\frac{\pi}{2}$ and the magnitude F_ℓ is fixed. As expected, we find that instability occurs when the load is predominantly in the $\mathbf{E}_2$ direction and the structure is stable when the terminal loading is vertical (cf. Figure 12).

It is of interest to see if the instability of the CNT structure can be tuned. With E, I, and W_{ad} associated with the intrinsic physical properties of the CNT, the separation width b is the only parameter that it is possible to control. Defining N_{cri} to be the maximum normal load for the

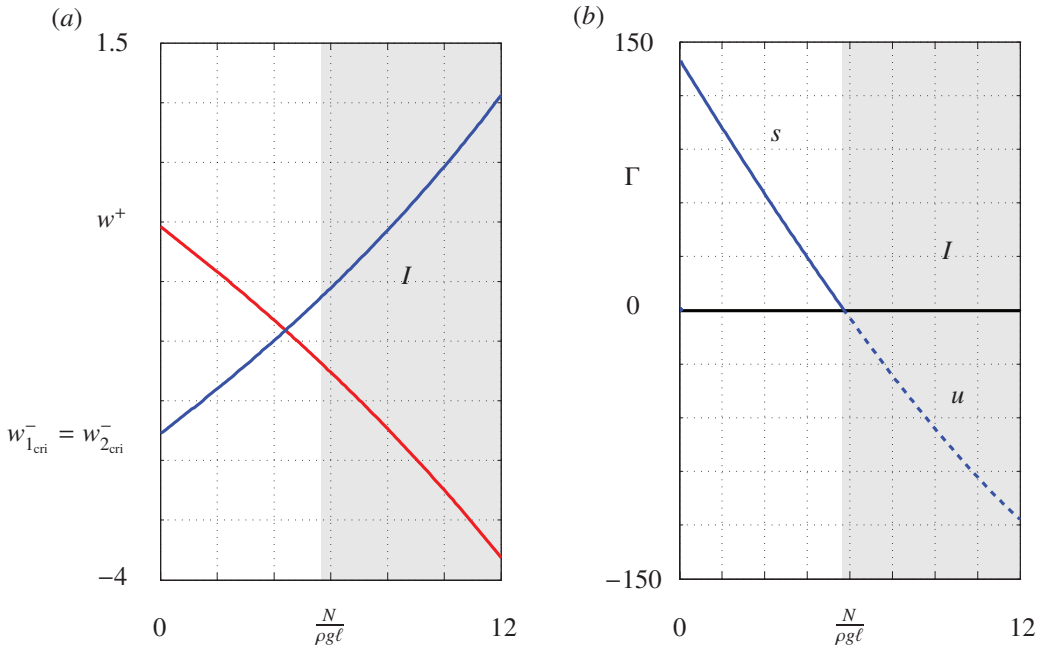

Figure 10: *Stability analysis of the fork-like structure loaded under its self weight and a normal load* $2N$*:* $\mathbf{F}_\ell = -2N\mathbf{E}_2$*. (a) The behavior of* w^+ *and* $w^-_{K_{crit}}$ *as a function of the dimensionless load* $N/\rho g\ell$*. (b) Maximum* Γ *found from the optimization problem (38). For the results shown,* $D = 1$*,* $\omega = 1$*, and* $\frac{b}{\ell} = 0.1$*. The shaded region labelled I indicates areas of the parameter space where* $\left(w_1^-, w_2^-\right) \notin \mathcal{F}$*, and the labels s and u indicate stability and instability, respectively.*

CNT pair to stay stable, and T_{cri} to be the maximum tangential load, we find that as b increases, N_{cri} decreases, whereas T_{cri} increases. These results are summarized in Figure 13. What is also evident from this figure is the increased strength of the adhered CNT structure compared to a pair of isolated CNTs carrying the same combined load. The curves shown in Figure 13 also indicate the tradeoff between increased tangential strength as b/ℓ increases with a decreasing compressive load bearing capability.

5. Bifurcation

To examine the usefulness of the stability criteria it is prudent to perform a bifurcation analysis and explore the possibility of stable solutions in the same parameter space as the solutions which have lost stability. To this end, we reexamine the situation where $\mathbf{F}_\ell = -2N\mathbf{E}_2$ and numerically explore if stable solutions are present after the structure has become unstable. These results are shown in Figures 2(a) and 14(a). As N increases from 0, a critical value N_c is reached where the forked configuration is no longer stable. Beyond the critical load it is possible that the forked structure unzips to form two separated rods. Indeed, if we examine the corresponding bifurcation diagram for a pair of separated rods each carrying a terminal load of $-N\mathbf{E}_2$, then we find that the straight configuration is stable for $N < N_s$. As N is increased beyond this value, the straight configuration is no longer stable and two buckled configurations are produced (cf.

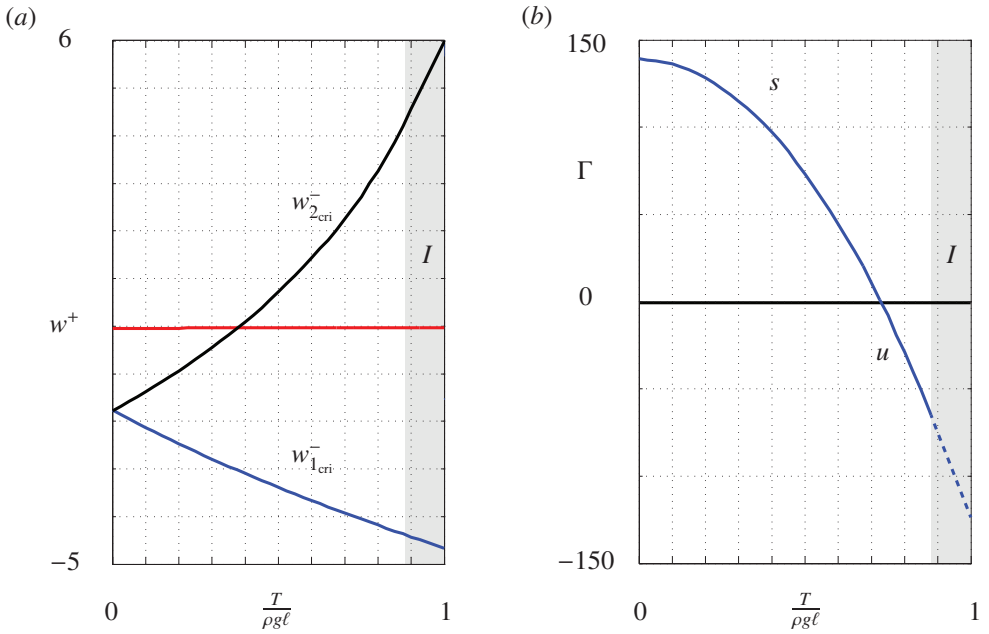

Figure 11: *Stability analysis of the fork-like structure loaded under its self weight and a tangential load* $\mathbf{F}_\ell = 2T\mathbf{E}_1$. *(a) The behavior of* w^+ *and* $w^-_{K_{crit}}$ *as a function of the dimensionless load* $T/\rho g\ell$. *(b) Maximum* Γ *found from the optimization problem (38). For the results shown,* $D = 1$, $\omega = 1$, *and* $\frac{b}{\ell} = 0.1$. *The shaded region labelled I indicates areas of the parameter space where* $\left(w_1^-, w_2^-\right) \notin \mathcal{F}$, *and the labels s and u indicate stability and instability, respectively.*

Figures 2(a) and 14(a)). The buckled configurations remain stable.[3]

It is interesting to examine the energetics of the aforementioned configurations. For this, we recall the expression for the total energy π of the fork structure (cf. (13)) and also consider the sum of the gravitational potential energy π_g, strain energy π_s and adhesion energy π_a of the rod. The sum of the latter three energies is equal to π minus the potential energy of the terminal load $\mathbf{F}_\ell$:

$$\pi_s + \pi_g + \pi_a = \pi - \pi_F, \tag{40}$$

where

$$\begin{aligned} \pi_F &= \int_\gamma^\ell p \mathrm{d}s + \sum_{J=1}^{2} \int_0^\gamma p_J \mathrm{d}s_J, \\ p &= 2N\sin(\theta) - 2T\cos(\theta), \\ p_1 &= (N+n)\sin(\theta_1) - (T+t)\cos(\theta_1), \\ p_2 &= (N-n)\sin(\theta_2) - (T-t)\cos(\theta_2). \end{aligned} \tag{41}$$

Referring to Figure 14, we observe that as the load N increases on the fork structure, its potential energy increase is entirely due to the load. When the stability criterion is violated as N increases

[3]For the individual unadhered CNTs, stability can be unambiguously established using the sufficient condition *LS* 1 discussed in [22, p.220].

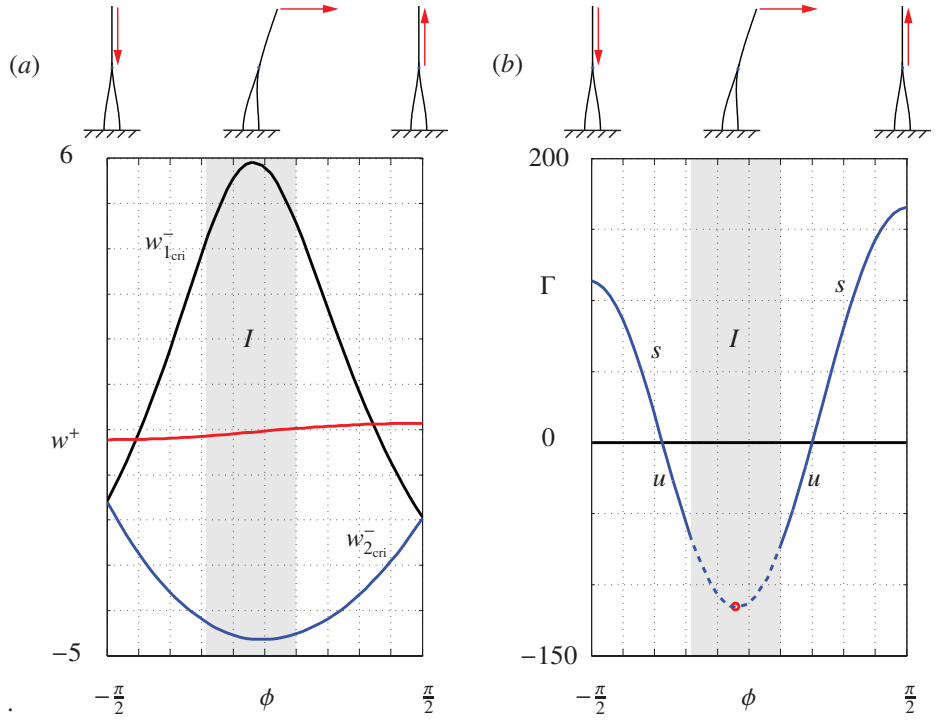

Figure 12: *Stability analysis for various loading configurations of the fork-like structure loaded under its self weight and a terminal load* $\mathbf{F}_\ell = F_\ell\,(\cos(\phi)\mathbf{E}_1 - \sin(\phi)\mathbf{E}_2)$. *(a) The behavior of* w^+ *and* $w^-_{K_{crit}}$ *as a function of the angle* ϕ. *(b) Maximum value* Γ *of (38). For the results shown,* $D = 1$, $\omega = 1$, $\frac{b}{\ell} = 0.1$, $\frac{F_\ell}{\rho g \ell} = 2$, *and* $\phi = \arctan\left(-\frac{N}{T}\right)$ *ranges from* $-\frac{\pi}{2}$ *to* $\frac{\pi}{2}$. *The shaded region labelled I indicates areas of the parameter space where* $\left(w_1^-, w_2^-\right) \notin \mathcal{F}$, *and the labels s and u indicate stability and instability, respectively.*

past N_c, a more energetically favorable configuration is available. This configuration features two buckled and unadhered rods. We also note, by comparing π and $\pi - \pi_F$ in Figures 14 (a) and (b), how the fork structure is able to absorb the energy of $\mathbf{F}_\ell$ without buckling for a far larger extent that the individual rods.

The corresponding situation where the load $\mathbf{F}_\ell$ is purely horizontal is summarized graphically in Figures 2(b) and 15. We observe from these figures that the unadhered rods do not buckle and that the contribution to the total energy π from the strain and gravitational energies increases as the load T is increased. It is also interesting to note from Figure 15(b) that the total energy π decreases as T is increased. For the fork structure, on the other hand, as the load $\mathbf{F}_\ell = 2T\mathbf{E}_1$ is increased, a critical load T_c is reached beyond which the stability criterion $AB1$ is violated. For loads beyond this value, the only neighboring stable configurations that we found correspond to a pair of unadhered rods. However, the total energy associated with the pair of rods is larger than that for the counterpart unstable fork structure, so any transition to the static stable state must be accompanied by a source of energy. This is clearly in contrast to the normal load case mentioned earlier. It is possible that a stable dynamic solution to the boundary value problem that is isoenergetic with the unstable fork structure at the critical load exists. However, our analysis is not capable of detecting such a solution.

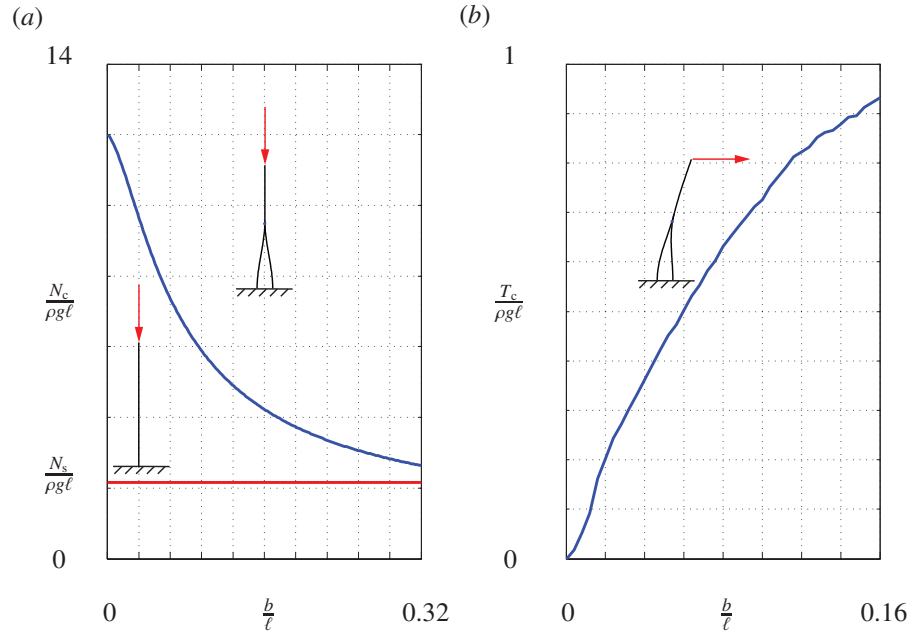

Figure 13: *Critical load analysis with a varying separation width b. (a) The corresponding critical normal dimensionless load* $\frac{N_c}{\rho g \ell}$ *as* $\frac{b}{\ell}$ *varies from* 0 *to* 0.32*. (b) The corresponding critical tangential dimensionless load* $\frac{T_c}{\rho g \ell}$ *as* $\frac{b}{\ell}$ *varies from* 0 *to* 0.16*. For the results shown,* $D = 1$ *and* $\omega = 1$*. The force* N_s *is the critical normal buckling load for a single CNT.*

6. Closing Remarks

We have established stability criteria for a pair of CNT struts which have the possibility of adhering through weak van der Waals interactions. The criteria are used to explore buckling and adhesion instabilities in these structures. In particular, from the results shown in Figures 14 and 15, we anticipate that instability is accompanied by a loss of adhesion and the fork-like structure unzips to form two stable yet unattached CNTs. If we were to consider a single CNT strut and load it beyond its buckling load, then the tip displacement will continuously change. In contrast with the adhered pair of CNT struts, the loss of stability is accompanied by a dramatic change in the tip displacement.

The short-range interaction forces in arrays of CNTs has also been found to play a role in other applications such as Gecko locomotion [28, 29, 20] and the mechanics of single cells [30]. In particular, it would be of interest to extend our present work to the branched hierarchical structure [31, 32] of the spatula and setae that feature in lizard locomotion. One could then use the resulting analysis to examine the role stability and instability plays in the attachment and detachment of spatula that branch from a single seta during locomotion. Such an extension would also serve to elucidate the benefits of the hierarchical structure that plays a predominant role in dry adhesion locomotion.

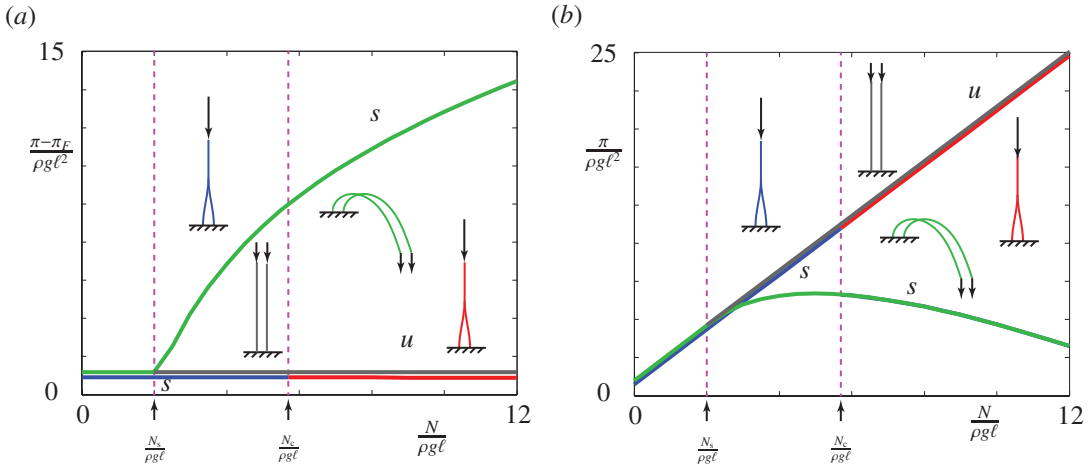

Figure 14: *Bifurcation diagram showing the dimensionless potential energies of the CNT pair under a normal load* $2N$*:* $\mathbf{F}_\ell = -2N\mathbf{E}_2$*. (a) The dimensionless potential energy* $\frac{\pi-\pi_F}{\rho g\ell^2}$ *composed of the strain energy, gravitational energy, and (where applicable) adhesion energy as* N *varies from* 0 *to* $12\rho g\ell$*. (b) The dimensionless potential energy* $\frac{\pi}{\rho g\ell^2}$ *composed of the strain energy, gravitational energy and terminal potential as* N *varies from* 0 *to* $12\rho g\ell$*. For the results shown,* $D = 1$*,* $\omega = 1$*, and* $\frac{b}{\ell} = 0.1$*. The labels* s *and* u *indicate stability and instability, respectively. The force* N_s *is the critical normal buckling load for a single CNT and the force* N_c *is the critical load for the forked structure.*

Acknowledgements

Xuance Zhou is grateful for the support of an Anselmo Macchi Fellowship for Engineering Graduate Students, a J.K. Zee Fellowship, and the Powley Fund for Ballistics Research. The authors are grateful to Professor Liwei Lin (U. C. Berkeley), Professor Jim Zuo (University of Illinois at Urbana Champaign) and Professor Yonggang Huang (Northwestern University) for providing the TEM image of CNTs. We also acknowledge numerous helpful discussions with Professor Carmel Majidi (Carnegie Mellon University).

References

[1] M. M. J. Treacy, T. W. Ebbesen, J. M. Gibson, Exceptionally high Young's modulus observed for individual carbon nanotubes, Nature 381 (1996) 678–680.
URL http://dx.doi.org/10.1038/381678a0

[2] R. H. Baughman, A. A. Zakhidov, W. A. de Heer, Carbon nanotubes–the route toward applications, Science 297 (5582) (2002) 787–792.
URL http://dx.doi.org/10.1126/science.1060928

[3] A. Christensen, J. Jacob, C. Richards, D. Bahr, R. Richards, Fabrication and characterization of a liquid-metal micro-droplet thermal switch, in: Transducers, Solid-State Sensors, Actuators and Microsystems, 12th International Conference on, 2003, Vol. 2, 2003, pp. 1427–1430.
URL http://dx.doi.org/10.1109/SENSOR.2003.1217043

[4] T. Zhang, S. Mubeen, N. V. Myung, M. A. Deshusses, Recent progress in carbon nanotube-based gas sensors, Nanotechnology 19 (33) (2008) 332001.
URL http://dx.doi.org/0957-4484/19/i=33/a=332001

[5] W. Oakley, E-Beam hard disk drive using gated carbon nano tube source and phase change media, in: Mass Storage Systems and Technologies, 2007. MSST 2007. 24th IEEE Conference on, 2007, pp. 245–250.
URL http://dx.doi.org/10.1109/MSST.2007.4367980

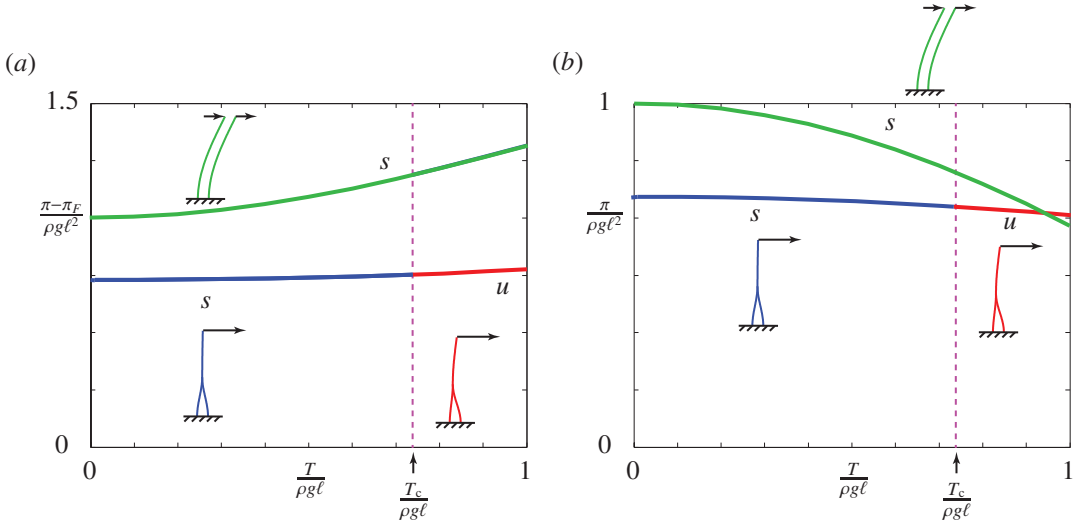

Figure 15: *Bifurcation diagram showing the dimensionless potential energies of the CNT pair under a tangential load* $2T$*:* $\mathbf{F}_\ell = 2T\mathbf{E}_1$*. (a) The dimensionless potential energy* $\frac{\pi-\pi_F}{\rho g\ell^2}$ *composed of the strain energy, gravitational energy, and (where applicable) adhesion energy as* T *varies from* 0 *to* $\rho g\ell$*. (b) The dimensionless potential energy* $\frac{\pi}{\rho g\ell^2}$ *composed of the strain energy, gravitational energy and terminal potential as* T *varies from* 0 *to* $\rho g\ell$*. For the results shown,* $D = 1$*,* $\omega = 1$*, and* $\frac{b}{\ell} = 0.1$*. The labels* s *and* u *indicate stability and instability, respectively. The force* T_c *is the critical load for the forked structure.*

[6] M. A. McCarthy, B. Liu, E. P. Donoghue, I. Kravchenko, D. Y. Kim, F. So, A. G. Rinzler, Low-voltage, low-power, organic light-emitting transistors for active matrix displays, Science 332 (6029) (2011) 570–573.
URL http://dx.doi.org/10.1126/science.1203052

[7] B. Chen, M. Gao, J. Zuo, S. Qu, B. Liu, Y. Huang, Binding energy of parallel carbon nanotubes, Applied Physics Letters 83 (17) (2003) 3570–3571.
URL http://dx.doi.org/10.1063/1.1623013

[8] W. Zhou, Y. Huang, B. Liu, K. C. Hwang, J. M. Zuo, M. J. Buehler, H. Gao, Self-folding of single- and multiwall carbon nanotubes, Applied Physics Letters 90 (7) (2007) 073107.
URL http://dx.doi.org/10.1063/1.2535874

[9] S. Cranford, H. Yao, C. Ortiz, M. J. Buehler, A single degree of freedom 'lollipop' model for carbon nanotube bundle formation, Journal of the Mechanics and Physics of Solids 58 (3) (2010) 409–427.
URL http://dx.doi.org/10.1016/j.jmps.2009.11.002

[10] H. Torabi, H. Radhakrishnan, S. D. Mesarovic, Micromechanics of collective buckling in CNT turfs, Journal of the Mechanics and Physics of Solids 72 (0) (2014) 144–160.
URL http://dx.doi.org/10.1016/j.jmps.2014.07.009

[11] R. A. Sauer, S. Li, An atomic interaction-based continuum model for adhesive contact mechanics, Finite Elements in Analysis and Design 43 (5) (2007) 384–396.
URL http://dx.doi.org/10.1016/j.finel.2006.11.009

[12] M. R. Falvo, G. J. Clary, R. M. Taylor, V. Chi, F. P. Brooks, S. Washburn, R. Superfine, Bending and buckling of carbon nanotubes under large strain, Nature 389 (1996) 582–584.
URL http://dx.doi.org/10.1038/39282

[13] T. Tong, Y. Zhao, L. Delzeit, A. Kashani, M. Meyyappan, A. Majumdar, Height independent compressive modulus of vertically aligned carbon nanotube arrays, Nano Letters 8 (2) (2008) 511–515.
URL http://dx.doi.org/10.1021/nl072709a

[14] A. N. Volkov, T. Shiga, D. Nicholson, J. Shiomi, L. V. Zhigilei, Effect of bending buckling of carbon nanotubes on thermal conductivity of carbon nanotube materials, Journal of Applied Physics 111 (5).
URL http://dx.doi.org/10.1063/1.3687943

[15] Y. Won, Y. Gao, M. A. Panzer, R. Xiang, S. Maruyama, T. W. Kenny, W. Cai, K. E. Goodson, Zipping, entanglement, and the elastic modulus of aligned single-walled carbon nanotube films, Proceedings of the National

Academy of Sciences 110 (51) (2013) 20426–20430.
URL http://dx.doi.org/10.1073/pnas.1312253110

[16] L. J. Sudak, Column buckling of multiwalled carbon nanotubes using nonlocal continuum mechanics, Journal of Applied Physics 94 (11) (2003) 7281–7287.
URL http://dx.doi.org/10.1063/1.1625437

[17] Q. Wang, W. H. Duan, K. M. Liew, X. Q. He, Inelastic buckling of carbon nanotubes, Applied Physics Letters 90 (3).
URL http://dx.doi.org/10.1063/1.2432235

[18] H. Shima, Buckling of carbon nanotubes: A state of the art review, Materials 5 (1) (2011) 47–84.
URL http://dx.doi.org/10.3390/ma5010047

[19] C. Majidi, O. M. O'Reilly, J. A. Williams, On the stability of a rod adhering to a rigid surface: Shear-induced stable adhesion and the instability of peeling, Journal of the Mechanics and Physics of Solids 60 (5) (2012) 827–843.
URL http://dx.doi.org/10.1016/j.jmps.2012.01.015

[20] C. Majidi, O. M. O'Reilly, J. A. Williams, Bifurcations and instability in the adhesion of intrinsically curved rods, Mechanics Research Communications 49 (0) (2013) 13–16.
URL http://dx.doi.org/10.1016/j.mechrescom.2013.01.004

[21] K. Hoffman, R. Manning, An extended conjugate point theory with application to the stability of planar buckling of an elastic rod subject to a repulsive self-potential, SIAM Journal on Mathematical Analysis 41 (2) (2009) 465–494.
URL http://dx.doi.org/10.1137/080731803

[22] O. M. O'Reilly, D. M. Peters, Nonlinear stability criteria for tree-like structures composed of branched elastic rods, Proceedings of the Royal Society A: Mathematical, Physical and Engineering Science 468 (2137) (2012) 206–226.
URL http://dx.doi.org/10.1098/rspa.2011.0291

[23] A. E. H. Love, A Treatise on the Mathematical Theory of Elasticity, 4th Edition, Cambridge University Press, Cambridge, 1927.

[24] N. A. Faruk Senan, O. M. O'Reilly, T. N. Tresierras, Modeling the growth and branching of plants: A simple rod-based model, J. Mech. Phys. Solids 56 (10) (2008) 3021–3036.
URL http://dx.doi.org/10.1016/j.jmps.2008.06.005

[25] O. M. O'Reilly, A material momentum balance law for rods, J. Elasticity 86 (2) (2007) 155–172.
URL http://dx.doi.org/10.1007/s10659-006-9089-6

[26] W. T. Reid, Riccati differential equations, Academic Press, New York, London, 1972.

[27] S. Boyd, L. Vandenberghe, Convex Optimization, Cambridge University Press, 2004.

[28] K. Autumn, Y. A. Liang, S. T. Hsieh, W. Zesch, W. P. Chan, T. W. Kenny, R. Fearing, R. J. Full, Adhesive force of a single gecko foot-hair, Nature 405 (2000) 681–685.
URL http://dx.doi.org/10.1038/35015073

[29] K. Autumn, M. Sitti, Y. A. Liang, A. M. Peattie, W. R. Hansen, S. Sponberg, T. W. Kenny, R. Fearing, J. N. Israelachvili, R. J. Full, Evidence for van der Waals adhesion in gecko setae, Proceedings of the National Academy of Sciences 99 (19) (2002) 12252–12256.
URL http://dx.doi.org/10.1073/pnas.192252799

[30] X. Zeng, S. Li, Multiscale modeling and simulation of soft adhesion and contact of stem cells, Journal of the Mechanical Behavior of Biomedical Materials 4 (2) (2011) 180 –189.
URL http://dx.doi.org/10.1016/j.jmbbm.2010.06.002

[31] B. Chen, P. Wu, H. Gao, Hierarchical modelling of attachment and detachment mechanisms of gecko toe adhesion, Proceedings of the Royal Society of London A: Mathematical, Physical and Engineering Sciences 464 (2094) (2008) 1639–1652.
URL http://dx.doi.org/10.1098/rspa.2007.0350

[32] Y. Tian, N. Pesika, H. Zeng, K. Rosenberg, B. Zhao, P. McGuiggan, K. Autumn, J. Israelachvili, Adhesion and friction in gecko toe attachment and detachment, Proceedings of the National Academy of Sciences 103 (51) (2006) 19320–19325.
URL http://dx.doi.org/10.1073/pnas.0608841103